

Evaluation of EGR techniques on a HSDI diesel engine using first law analysis

Nick Papaioannou^{1*}, Felix C.P. Leach¹, Martin H. Davy¹, Adam Weall², Brian Cooper²

¹ Department of Engineering Science, University of Oxford, Oxford, OX1 3PJ, UK

² Jaguar Land Rover Ltd. Coventry, CV4 7HS, UK

*Corresponding Author: nick.papaioannou@eng.ox.ac.uk

Abstract

The effects of different EGR strategies on engine efficiency and the resulting energy flows at two speed/load conditions (1500 rpm/6.8 bar nIMEP and 1750 rpm/13.5 bar nIMEP) were studied using a first law analysis approach. The EGR strategies tested were: cooled high-pressure EGR (baseline), the application of EGR with the swirl flap closed and the use of EGR under constant λ conditions. The closed swirl flap EGR strategy reduced brake efficiency under high load conditions and increased heat transfer to the coolant for both load cases. Soot and CO emissions increased at high load, however with an increase in NO_x relative to the baseline case. The constant λ EGR strategy reduced brake efficiency under low load, as well as the heat flow to the coolant for both load cases. The constant λ EGR strategy benefits smoke emissions and increases combustion EGR tolerance, albeit with a penalty in NO_x emission.

Introduction

The use of diesel vehicles has significantly increased in the past decade such that diesel vehicles now account for approximately 50% of the total passenger vehicles sold in Europe [1]. The increased demand for diesel vehicles is due, for the most part, to the diesel's higher efficiency compared to their gasoline counterparts. However, emissions compliance costs are significantly higher for diesels – with almost half the diesel's compliance costs being associated with the exhaust after-treatment system [2]. Enhancing the efficacy of existing emission reduction techniques – such as exhaust gas recirculation (EGR) for NO_x reduction – therefore has the potential to reduce the overall cost of the diesel vehicle.

The use of EGR in diesel engines as a method of NO_x reduction, by displacing fresh intake charge, is widely covered in the literature [3-8]. Thermal NO_x emissions are reduced due to the reduced oxygen concentration in the cylinder and the presence of inert gases with higher heat capacity both of which act to lower combustion temperatures. However some care is required, reduced oxygen concentrations and lower in-cylinder temperatures may also reduce oxidation rates to the point that soot, CO, and THC emissions are increased—a tendency that may be offset by increasing mixing rates. Higher levels of in-cylinder swirl, the bulk rotation of the charge about the cylinder axis that is induced during induction, have been shown to reduce the emissions penalty traditionally associated with EGR. Increasing swirl enhances local fuel-air mixing leading to improved combustion efficiency and emissions oxidation [9]—albeit with potential penalties in NO_x emissions and volumetric efficiency [10], [11]. However, excessive levels of swirl can reduce thermal efficiency due to increased convection losses, slowing combustion and increasing CO and THC emissions [9], [11], [12], [13].

In this study, a detailed first law analysis (FLA) modelling tool has been developed which has been used to assess the energy flows and efficiency of three different cooled high-pressure EGR methods at two different operating conditions (1500 rpm/6.8 bar nIMEP and 1750 rpm/13.5 bar nIMEP). The three EGR methods examined were; a baseline high-pressure (HP) EGR case, HP EGR with increased swirl, and HP EGR under constant λ conditions. Note that while FLAs on internal combustion engines are not new, with many examples available in the literature [14-

23], the application of FLA to EGR application methods is novel and the results of this work are expected to guide the development of future EGR strategy.

Experimental facility

Engine

This study was performed on a single cylinder diesel engine supplied by Jaguar Land Rover. The base is a Ricardo Hydra research engine and the combustion chamber, cylinder head and crank-piston assembly are based on the Jaguar Land Rover AJ200D “Ingenium” engine [24]. A production standard fuel injection system is used. The specifications of the engine along with the properties of the fuel used can be seen in Table 1. The engine is equipped with a split cooling system, allowing for independent cooling of the cylinder head and the jacket and a high pressure EGR loop. A VDO brand throttle is fitted in the filling port approximately 15 cm upstream of the intake valve so as to provide control of in-cylinder swirl. Closing the intake port throttle, hereafter described as the swirl flap, increases swirl levels in the cylinder as documented in a previous work [11]. A schematic of the single cylinder engine and the engine instrumentation measurement points is given in Figure 1.

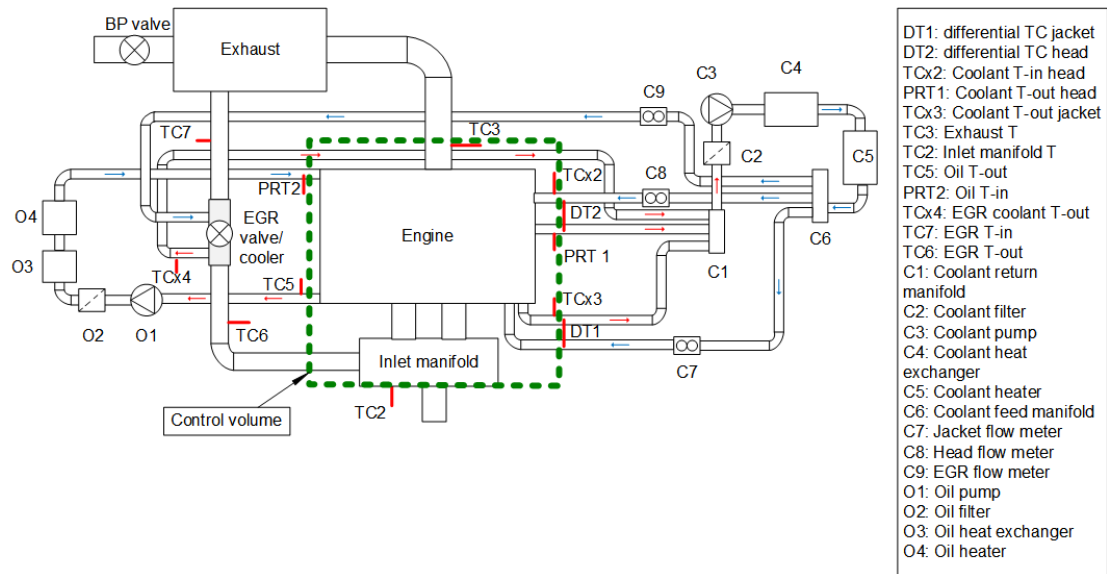


Figure 1: Schematic of experimental equipment used.

Table 1: Engine, injection system and fuel specifications

Parameter	Specification
Bore \times Stroke	83 \times 92.4 mm
Displacement	500 cm ³
Valves per Cylinder	2 intake, 2 exhaust
Compression Ratio	15.4 : 1
Injection system	Common rail
Fuel Pressure	400-1800 bar
Injector holes	8
Fuel Cetane number	52
Fuel Sulphur content	6.5 mg/kg
Fuel LHV	42.7 KJ/g

Test Cell Instrumentation

The engine was driven by a 57 kW VASCAT AC dynamometer and an ABB Power Electronics unit controlled by a Sierra-CP Engineering “Cadet” engine control system. Dedicated conditioning units control the coolant and oil supply temperatures to the engine to ± 1 K. Boosted intake conditions are provided by a set of external compressors capable of providing a total of 4.5 bar absolute pressure at full speed conditions. The intake pressure is regulated with an accuracy of ± 0.5 % by a PID controlled dump valve system. An external 10 kW heater (OSRAM Sylvania) and a 15 kW chiller (International Celsius) provided intake air temperature control with ± 1 K accuracy. The exhaust system was equipped with a 25 L smoothing tank to reduce the pulsations found in single cylinder engines. A closed-loop controlled exhaust back pressure valve (BPV) was mounted downstream of the smoothing tank.

The individual coolant volume flow rates for the cylinder head, cylinder jacket and EGR engine cooling circuits were measured with turbine flowmeters by TITAN Enterprises with an accuracy of 0.7 % reading or 0.08 L/min. The oil volume flow rate was measured using a FLOMEC oval gear flowmeter with an accuracy of ± 0.6 % reading or ± 0.22 L/min. Fuel flow measurement was provided by a Sierra-CP FuelTrak 1000 gravimetric fuel weigher with an accuracy of ± 0.05 % of the reading, or ± 0.03 g.

A Pi Innovo M670 OpenECU, which is based on a Jaguar Land Rover (JLR) Simulink model, was used for engine and fuel system control. A Horiba MEXA-ONE emissions analyser [25] was used for emission analysis along with an AVL415S smoke meter unit [26]. An AVL Indicom high-speed data acquisition system was used to log in-cylinder pressure, intake port pressure, exhaust pressures and the injector current

clamp signal at a resolution of 0.1 CAD. Low speed data logging at 1 Hz was provided by the Cadet control system. More detail about the test cell and its instrumentation can be found in [27].

Differential thermocouples

The cylinder head and the cylinder jacket cooling circuits were fitted with high accuracy differential K-type thermocouple systems, purpose built for the present study, with the reference thermocouples (i.e. the cold junction) installed into the feed lines as shown in Figure 2.

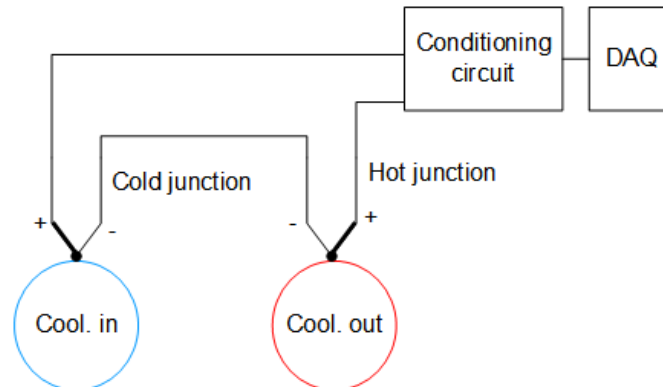


Figure 2: On-engine configuration of differential thermocouples

Due to the small differential voltage signal between the two thermocouples, two stages of amplification were used. Due to the negative temperature differences observed across the engine at some low load conditions (i.e. the coolant was heating the engine at these points), a DC offset voltage was applied to bring the measured signal within the data acquisition input signal range. (0-10 V). With regards to the additional uncertainty potentially induced by the addition of the DC offset, particular care was taken to ensure supply voltage stability. The differential thermocouples were calibrated “offline” using two water baths; the reference bath was held at a constant temperature of 90°C to simulate the operating conditions of the engine. The calibration procedure included testing at negative temperature differentials with the offset voltage applied. The 95% confidence limit of the calibrated sensitivity was 0.6% and 1% for the two differential thermocouple systems. The measurement uncertainty for the system shown in Table 2 is the maximum measurement uncertainty at the 95% confidence interval encountered in the experiments presented here.

Table 2: Differential thermocouples’ specifications

Parameter	Range
Differential temperature range	-4 K to 12 K
Uncertainty	± 0.07 K - 95% confidence
Output signal range	0-10 V
Supply voltage	12 V

Experimental Methodology

Test plan and operating conditions

Six EGR sweeps were performed across the three different EGR application strategies and two different load conditions. Each EGR sweep was at three EGR levels, 0%, 17%, and 22% or 35% depending on load condition (the maximum EGR rate was limited by an upper limit of filter smoke number (FSN), where FSN is a measure of sooted filter paper opacity). Table 3 details the engine operating conditions for each EGR strategy and load point.

Table 3: Operating conditions for the two load cases.

Test point	1500 rpm/6.8 bar			1750 rpm/13.5 bar		
Engine speed (rpm)	1500			1750		
Fuel rail pressure (MPa)	55			90		
Inlet air temperature (°C)	40			40		
Coolant temperature (°C)	90			90		
EGR strategy – Baseline/Swirl flap closed						
Intake pressure (barG)	0.25			1.0		
Exhaust pressure (barG)	0.45			1.4		
nIMEP (bar)	6.8			13.5		
Intake Y _{O₂} (EGR %v/v)	0.23 (0 %)	0.21 (17 %)	0.18 (35 %)	0.23 (0 %)	0.20 (17 %)	0.19 (22 %)
EGR strategy – Constant λ						
Intake pressure (barG)	0.25	0.40	0.70	1.0	1.4	1.5
Exhaust pressure (barG)	0.45	0.70	1.2	1.4	1.8	2.1
nIMEP (bar)	6.8	6.7	6.5	13.5	13.5	13.4
Intake Y _{O₂} (EGR %v/v)	0.23 (0 %)	0.22 (17 %)	0.19 (35 %)	0.23 (0 %)	0.21 (17 %)	0.20 (22 %)

There are several points of note with respect to the engine's operation at the conditions detailed in Table 3. The air flow rate into the engine was controlled by fixing both inlet and exhaust pressures as shown—the pressure differential across the manifolds provided the driving force for EGR delivery with the EGR rate being controlled independently of the driving pressure using an EGR valve (refer to Figure 1). For the constant λ EGR points, it was necessary to increase the inlet and exhaust pressures from the baseline condition as shown in Table 3 so as to maintain the target λ value at a given EGR rate—with the exhaust pressure increasing more rapidly than the intake pressure. The intake temperature was held constant at 40°C for all test points, in order to remove thermal throttling effects (i.e. the reduction of volumetric efficiency due to lower charge density) typically associated with the use of EGR.

Constant start of injection timings (pilot and main) were maintained across all test points in order to allow the identification of the effects of EGR strategies on combustion progression. For the Baseline and SF closed cases, main injection fuelling was adjusted to maintain a constant net indicated mean effective pressure (nIMEP) at each load condition. However, for the constant λ cases, the fuelling was kept constant at the baseline (0% EGR) level as EGR rate was increased, resulting in a reduction of nIMEP with EGR as indicated in the table.

Experimental procedure, data analysis and reporting

For each engine test point the engine was run at the target speed and load until steady state conditions of coolant and oil temperature were established. Thereafter, low-speed (1 Hz) data from each experiment were logged for a period of three minutes. High-speed (0.1 CAD) combustion data were logged for 300 consecutive cycles. A minimum of three independent experiments were performed at each test point and a mean data set was generated for each condition.

Energy flows for the engine were calculated using the first law model that is described in Appendix A. The model was coded in Matlab and applied to the mean data sets from the experiments. The model gives nine energy flow outputs that are presented in percentage terms relative to the total energy input into the system (i.e. the chemical energy of the fuel plus the enthalpy of the intake charge). The model outputs are: brake work (which, following the definition above, is the same as brake efficiency), heat flow to coolant in the cylinder jacket, heat flow to the coolant in the head, heat flow to the oil, exhaust enthalpy, exhaust chemical energy, fuel pump energy, and extraneous losses. The extraneous term accounts for all of the energy transfer that cannot be measured with the currently installed instrumentation, primarily heat transfer across the control volume boundary, in the form of radiation and convection losses from the engine itself. Smith et al. [22] have shown that an “adiabatic” enclosure around the engine can be used to measure this term; however the use of such an enclosure was not feasible in this work due to space limitations within the test cell. Full details of the model and the extraneous losses are given in Appendix A. The measurement locations relative to the system control volume are presented in Figure 1.

Combustion related performance metrics for temperature, heat release and mass fraction burned (MFB) were calculated from mean in-cylinder pressure data using an industry standard combustion analysis package, AVL Concerto. Bulk gas temperature

was calculated using the properties of pure, dry air with an empirically determined coefficient to account for the modified mixture properties due to the fuel present in the cylinder and a varying specific heat ratio (γ) based on temperature [28]. Values of MFB are presented with respect to the start of pilot injection.

The mass flow rate of the exhaust gases was calculated from the sum of the mass of the exhaust species, based on the number of moles and their molar mass. The number of moles was calculated from the iterative solution of five simultaneous equation based on the method presented by Silvis [29]. This calculation also accounts for species that are not directly measured by the emission analyser and thus provides a more complete indication of the exhaust chemical energy.

All figures and graphs presented in this work show the mean experimental data points. So as to allow fair comparison between operating strategies, energy flows are presented graphically against the intake charge composition expressed in terms of intake oxygen mass fraction (Equation 1).

$$Y_{O_2[intake]} = \frac{m_{O_2[fc]} + m_{O_2[exh]}}{m_{fc} + m_{EGR}} \quad (1)$$

where $m_{O_2[fc]}$ is the oxygen mass of the fresh charge, $m_{O_2[exh]}$ is the oxygen mass in the EGR gases and m_{fc} and m_{EGR} is the mass of the fresh charge and the mass of EGR respectively. The relationship between EGR rate and Y_{O_2} for the conditions tested is shown in Table 3.

In all cases error bars show the 95 % confidence limits of the mean data. Where error bars are not visible, the 95 % confidence limit is sufficiently small as to be hidden by the data marker. Finally, all emission results are presented as normalised values, with the exception of Figure 16, where NO_x emissions are given relative to the highest value measured across the full test matrix.

Results and discussion

Overall energy balance and brake work

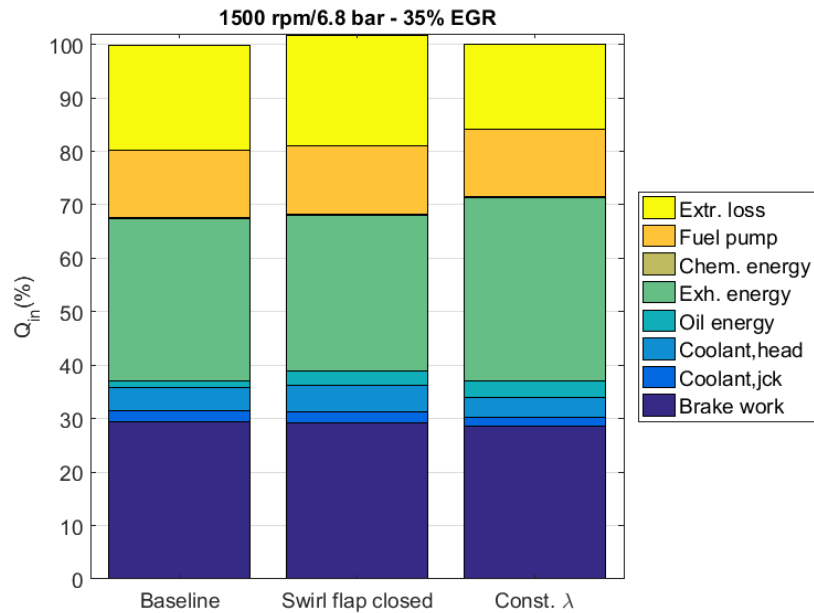


Figure 3: Energy balance results (normalised with respect to the total energy input to Baseline) for the different EGR strategies under 1500 rpm/6.8 bar nIMEP, 35 % EGR rate conditions.

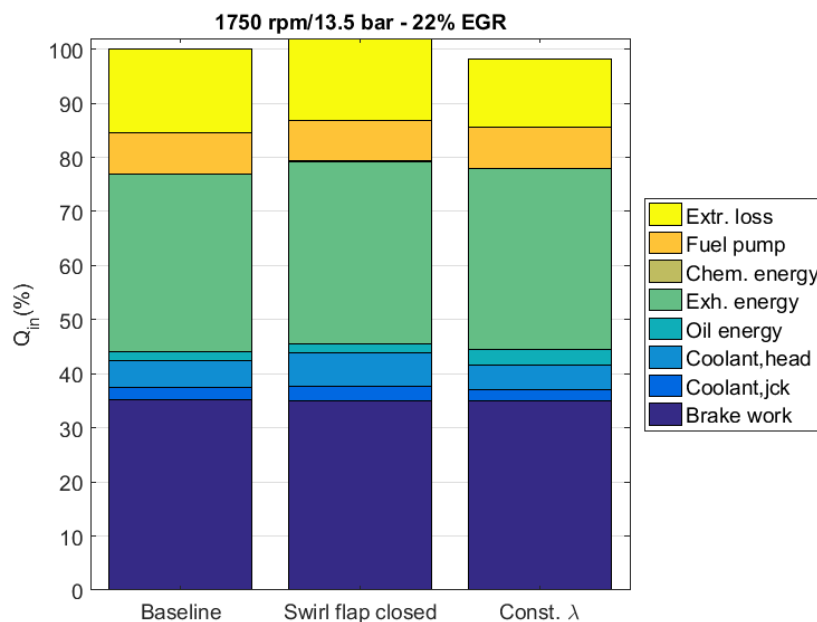


Figure 4: Energy balance results (normalised with respect to the total energy input to Baseline) for the different EGR strategies under 1750 rpm/13.5 bar nIMEP, 22 % EGR rate conditions.

Figures 3 and 4 present sample energy balance results for both load/speed conditions at their respective highest EGR rates (i.e. 35 % and 22 %, as shown in Table 3). Similar trends were observed between the different EGR strategies for all EGR rates and load conditions and are thus not presented for clarity. The results indicate that the two major energy transfers terms, independent of EGR strategy, are brake work and exhaust thermal energy. Note that the pumping work (quantified for each test point in Figure 5) is included in the brake work term as the output from the dynamometer load cell represents the net effect of the useful work during the power stroke and the work consumed during the gas exchange process.

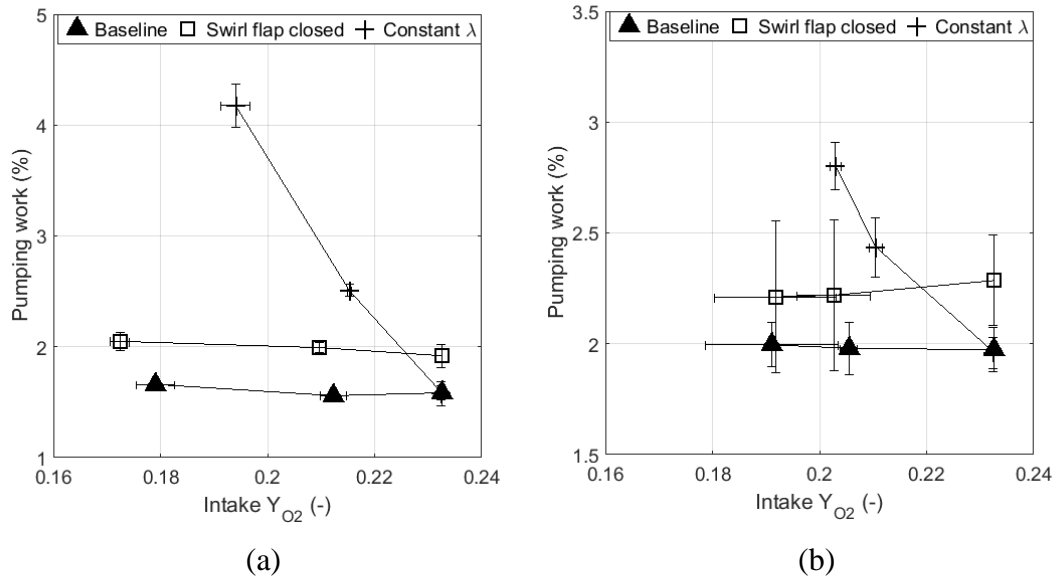
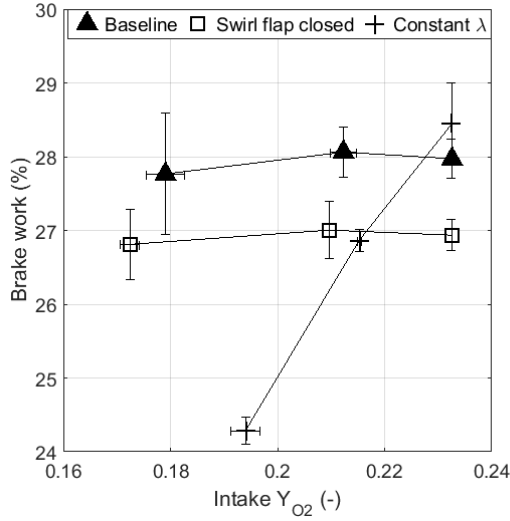
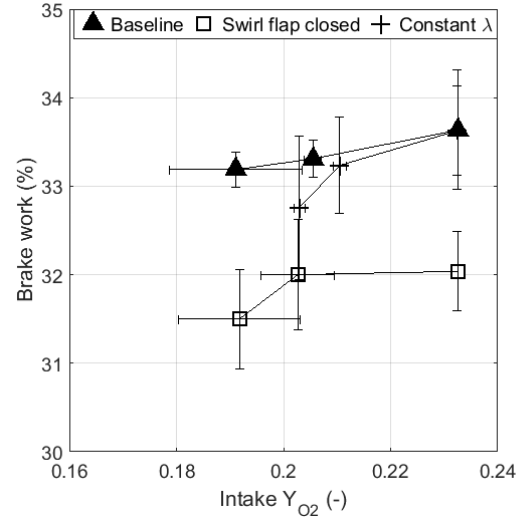


Figure 5: Pumping work as a percentage of input energy vs. intake oxygen mass fraction for the different EGR strategies at (a) 1500 rpm/6.8 bar nIMEP and (b) 1750 rpm/13.5 bar nIMEP load conditions.

Extraneous losses, which are dominated by convective and radiative heat transfers from the hot surfaces of the engine to the ambient air [22], are the third most significant energy transfer terms in the results. A comparison between the two load cases indicates that the extraneous losses are reduced at higher load conditions independent of EGR strategy. This is due to the larger injected fuel mass at higher load which reduces the relative proportion of extraneous losses with respect to the total energy input despite an increase in engine surface temperature.

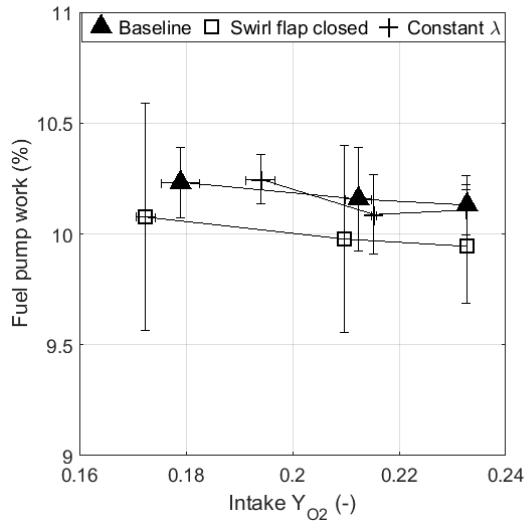


(a)

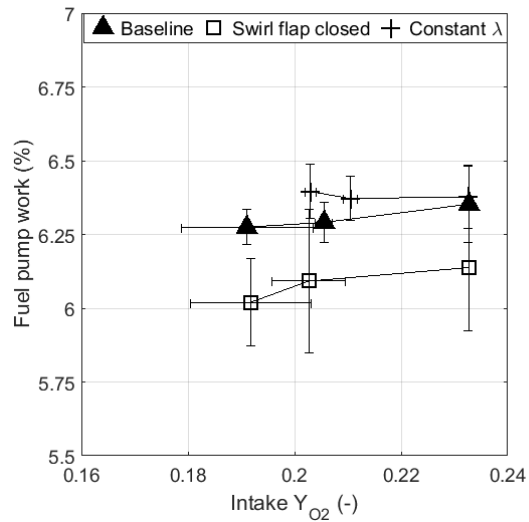


(b)

Figure 6: Brake work out vs. intake oxygen mass fraction for the different EGR strategies at (a) 1500 rpm/6.8 bar nIMEP and (b) 1750 rpm/13.5 bar nIMEP load conditions.



(a)



(b)

Figure 7: Fuel pump work as a percentage of input energy vs. intake oxygen mass fraction for the different EGR strategies at (a) 1500 rpm/6.8 bar nIMEP and (b) 1750 rpm/13.5 bar nIMEP load conditions.

Figure 6 presents the variation of brake work output with intake oxygen mass fraction under the different operating conditions. It is clear that under 1500 rpm/6.8 bar nIMEP conditions, the brake work is decreased significantly (~4-7 %) compared to the 1750 rpm/13.5 bar nIMEP case. This decrease is attributed to relatively increased fuel pump work (the sole ancillary loss on this engine) shown in Figure 7. Note that the fuel pump that was used in this work was sourced from a production four-cylinder

engine and was run with the Volume Control Valve (VCV) disabled. Hence, the magnitude of the pump loss is significantly higher than would be expected on a production engine. The parasitic torque used for the calculations was 8.5 Nm based on published data for a high-pressure diesel pump [30]. These data were corrected to account for the differences in pump types between the two studies.

Measurement of heat transfer to the coolant system

Figure 8 presents the total energy transferred to the coolant vs. intake oxygen mass fraction for all three EGR strategies. Increasing the EGR rate (reducing intake oxygen mass fraction) reduces the heat transferred to the cooling system at both speed/load conditions regardless of EGR strategy. However, the reductions are small and the results are not statistically significant at the 95 % confidence interval with 3 repeated tests. Nonetheless the trends are consistent and are attributed by the authors to the reduction of bulk gas temperature at higher EGR conditions (as shown in Figure 15).

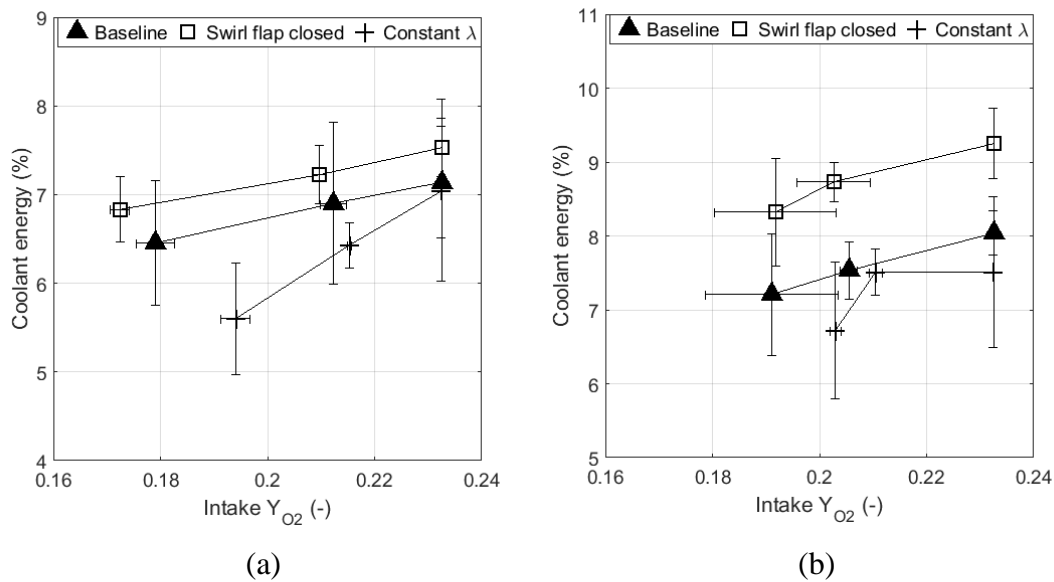


Figure 8: Total heat transferred to the coolant as a percentage of input energy vs. intake oxygen mass fraction for the different EGR strategies at (a) 1500 rpm/6.8 bar nIMEP and (b) 1750 rpm/13.5 bar nIMEP load conditions.

The magnitude of the error bars shown in Figure 8 well illustrate the difficulty of accurately determining coolant heat flows on a single cylinder engine. Under low load conditions, the typical rise in coolant temperature across the engine is approximately 0.8 K. Thus, even with high accuracy differential thermocouple systems with measurement uncertainties as low as ± 0.07 K, such as those used in the current study, the percentage error in the temperature measurements is approximately 9%. If standard K-type thermocouples, calibrated to ± 0.25 K, were to be used for these measurements then the uncertainty in the measured temperature differential across the engine would approach 45%. If it is assumed that the standard deviation of the current work is representative of a larger sample, then the results indicate that a further 23 tests with the high-accuracy differential thermocouple system would be required to provide statistical certainty to the low-load measurements at the 95% confidence level. Assuming a standard deviation of 0.6 K for the K-type thermocouple

measurements suggests that achieving statistically meaningful results at the 95% confidence interval would require many hundreds of individual tests.

Swirl flap effects

It is well understood from literature, e.g. [10], [11], that the throttling effect of closing a swirl flap will increase pumping work and reduce brake efficiency as indicated in Figures 5 and 6. It is also expected that efficiency will be affected by swirl flap induced changes to the mixing, combustion and heat transfer characteristics of the engine.

Figure 8 shows that closing the swirl flap increases the total heat flow to the coolant independent of load. This result is consistent with current understanding of swirl flap effects; closing a swirl flap increases in-cylinder swirl mixing, leading to faster burning and higher in-cylinder temperatures [12], [31]. In addition, the increased mean flow velocity and turbulent intensity associated with swirl flap use increases convective heat transfer [9], [13], [31]. Both of these effects are expected to increase the heat flux to the cylinder wall and thus the heat transferred to the coolant. Detailed examination of emissions and heat release results provides further insight into the causes of the increased heat transfer to the coolant when the swirl flap is closed. Figure 9 shows the NO_x -smoke results for the different operating conditions.

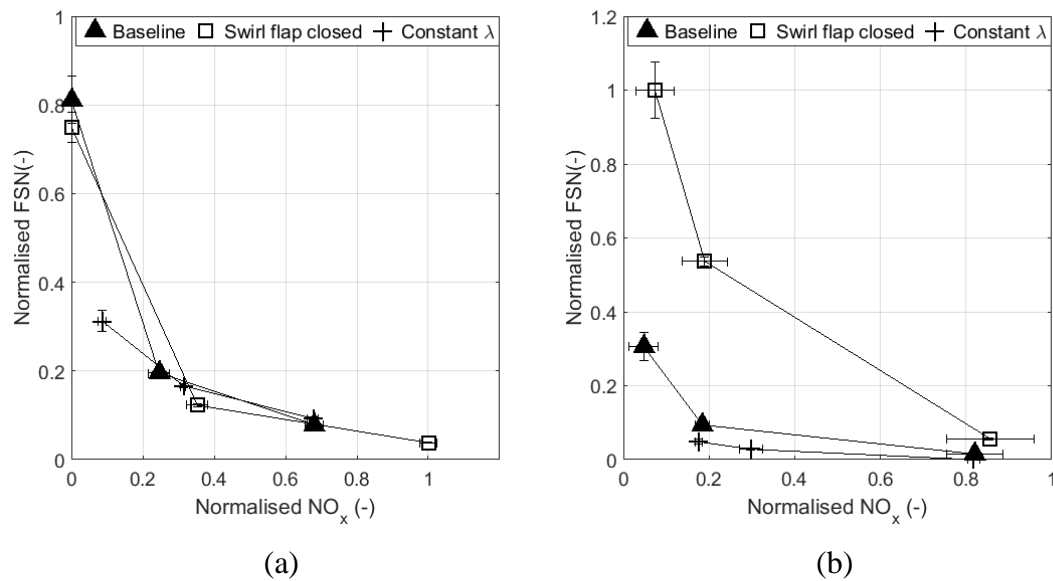


Figure 9: Normalised NO_x vs normalised filter smoke number (FSN) for the different EGR strategies at (a) 1500 rpm/6.8 bar nIMEP and (b) 1750 rpm/13.5 bar nIMEP load conditions.

1500 rpm/6.8 bar nIMEP load condition

At the low-load 1500 rpm/6.8 nIMEP condition, higher NO_x emissions with the closed swirl flap at 0 % and 17 % EGR suggest higher combustion temperatures relative to the baseline case, consistent with the literature [12,13]. For the 35 % EGR case, the NO_x results are essentially independent of swirl flap position – perhaps indicating that the in-cylinder temperature in both of these high EGR cases is sufficiently low as to inhibit any significant ‘thermal’ NO_x production. Closing the swirl flap is shown to increase ignition delay, approximated throughout this work by the crank angle duration between start of pilot injection (SOI.P) and the angle of 5% mass fraction burned (CA5), for all EGR rates as seen in Figures 10(a). The corresponding data for combustion phasing and duration, presented in Figures 11(a) and 12(a) respectively, show that the combustion event is advanced and overall combustion duration is decreased compared to the baseline case—indicating a beneficial increase in post-ignition fuel-air mixing resulting in reduced smoke, CO, and THC emissions as shown in Figures 9(a), 13(a), and 14(a) respectively.

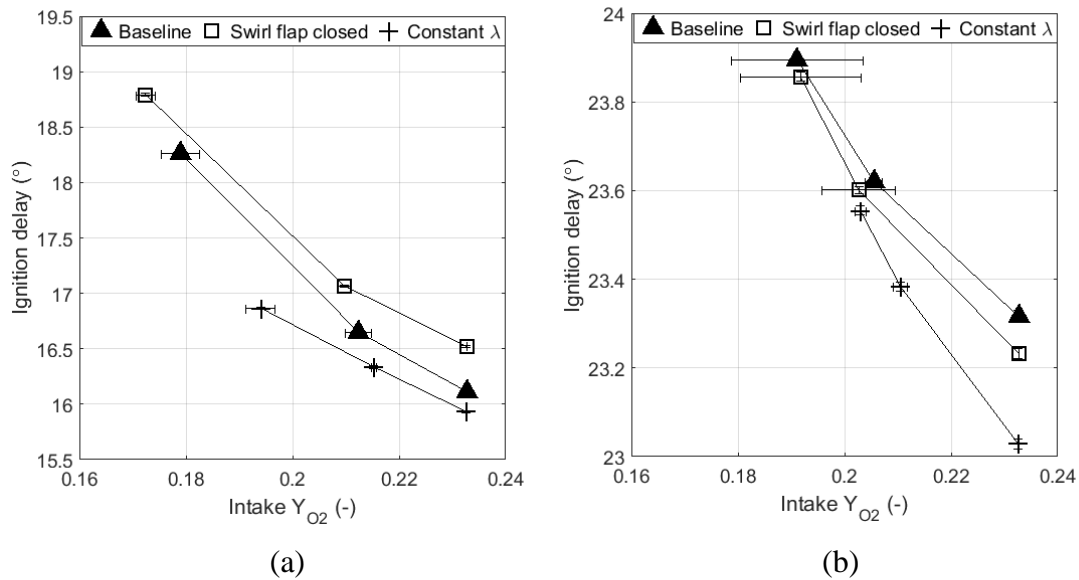
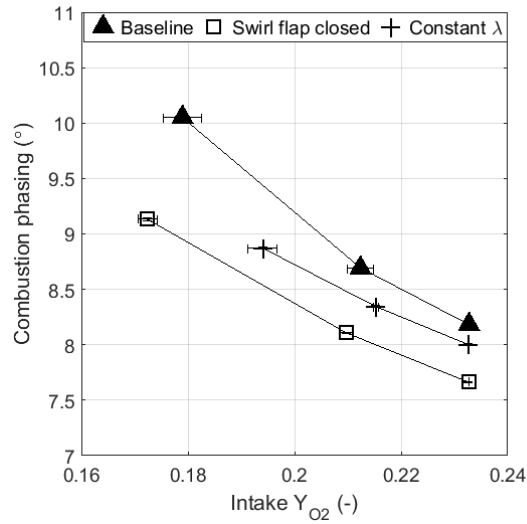
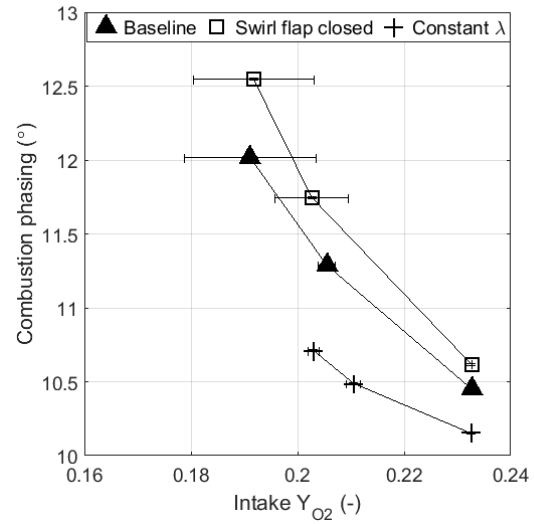


Figure 10: Ignition delay (CA5 – SOI.P) vs. intake oxygen mass fraction for the different EGR strategies at (a) 1500 rpm/6.8 bar nIMEP and (b) 1750 rpm/13.5 bar nIMEP load conditions.

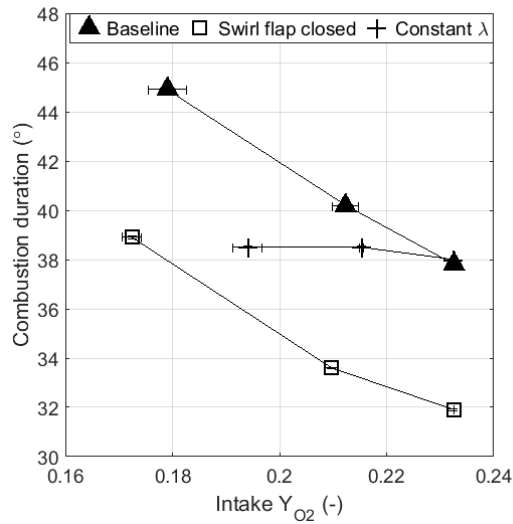


(a)

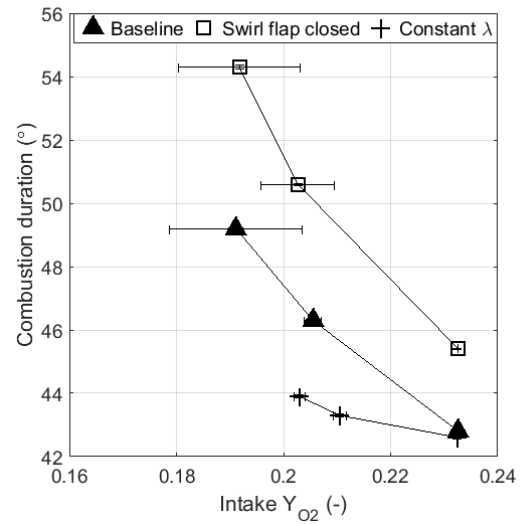


(b)

Figure 11: Combustion phasing (CA50 – TDC) vs. intake oxygen mass fraction for the different EGR strategies at (a) 1500 rpm/6.8 bar nIMEP and (b) 1750 rpm/13.5 bar nIMEP load conditions.

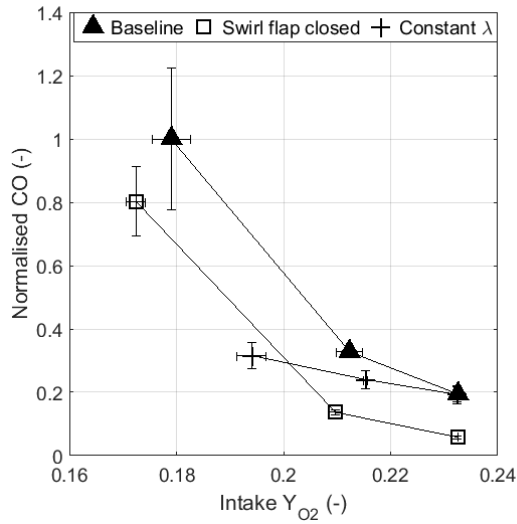


(a)

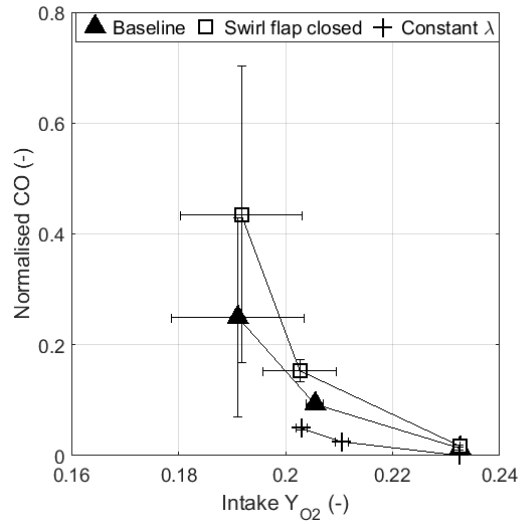


(b)

Figure 12: Combustion duration (CA90 - SOLP) vs. intake oxygen mass fraction for the different EGR strategies at (a) 1500 rpm/6.8 bar nIMEP and (b) 1750 rpm/13.5 bar nIMEP load conditions.

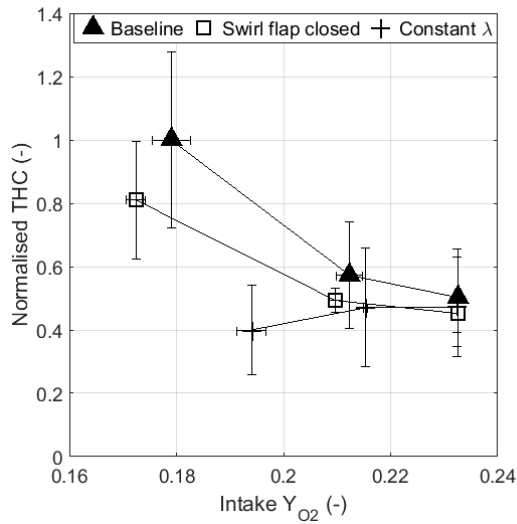


(a)

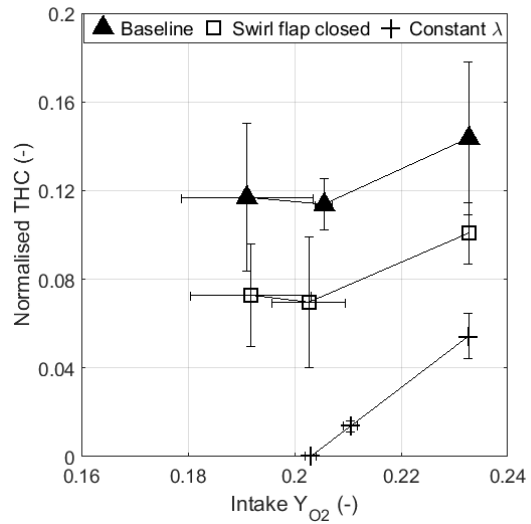


(b)

Figure13: Normalised CO emissions vs. intake oxygen mass fraction for the different EGR strategies at (a) 1500 rpm/6.8 bar nIMEP and (b) 1750 rpm/13.5 bar nIMEP load conditions.



(a)



(b)

Figure 14: Normalised THC emissions vs. intake oxygen mass fraction for the different EGR strategies at (a) 1500 rpm/6.8 bar nIMEP and (b) 1750 rpm/13.5 bar nIMEP load conditions.

1750 rpm/13.5 bar nIMEP load condition

At the higher speed/load condition however, we see a different situation. In-cylinder swirl is known to scale with engine speed [32]. Therefore, the baseline swirl level is expected to be higher at the 1750 rpm/13.5 bar nIMEP condition than at 1500 rpm/6.8 bar nIMEP operating point. Closing the swirl flap will increase this swirl level still further. Excessive levels of swirl have been reported to increase heat convection, which can lead to lower cylinder temperatures and longer combustion durations [32-34]. This extended combustion duration can lead to incomplete combustion due to flame quenching – increasing soot, CO and THC emissions [31], [34], [35]. High levels of cylinder swirl can also lead to fuel jet-jet interactions increasing local equivalence ratio and consequently CO and THC emissions [13], [35].

The results presented in Figures 11(b) and 12(b) do show an increase in combustion duration when the swirl flap is closed at the higher load condition. Soot and CO emissions also increase (Figures 9(b) and 13(b)) consistent with a reduction in soot oxidation and incomplete oxidation of fuel due to flame quenching. However, THC emissions at this load point are relatively insensitive to both swirl flap position and EGR rate (Figure 14(b)). One possible explanation for these seemingly contradictory results could be that the CO emissions at this load point are dominated by the late cycle bulk quenching effects whereas THC emissions are, to a significant degree, due to over-leaning of the fuel-air mixture at the periphery of the spray prior to ignition. Considering the ignition delay, Figure 10(b) indicates a reduced sensitivity to EGR compared to the lower speed/load condition. This is consistent with the increased swirl motion associated with higher engine speed improving fuel-air mixing and hence offsetting the oxygen displacement effect of increasing EGR. A notable feature of the ignition delay data at the 1750 rpm/13.5 bar nIMEP condition (Figure 10(b)) is its relative insensitivity to the swirl flap position, which is reflected in the THC results.

Taken as a whole, the emissions trends presented in Figures 9, 13 and 14 indicate that the increases in coolant heat flow relative to the baseline condition shown in Figure 8 when the swirl flap closed are the result of significantly different physical phenomena for the two speed/load conditions. For the lower speed/load case, the emissions results suggest that the increased heat flow to the coolant is predominantly due to higher in-cylinder temperatures. For the higher speed/load case, the emissions results suggest that the cause is likely an increase in the convective heat transfer coefficient compensating for a reduction in the in-cylinder gas temperature. Note that the calculated peak bulk gas temperatures presented in Figure 15 do show an increase from the baseline value with swirl flap operation for the 1500 rpm/6.8 bar nIMEP low load case and a decrease for the higher speed/load (1750 rpm/13.5 bar nIMEP) case. However, it should be noted also that the results presented in Figure 15 indicate the combined effects of varying charge properties and in-cylinder motion along with the effects of variable combustion phasing for the different EGR strategies and EGR rates.

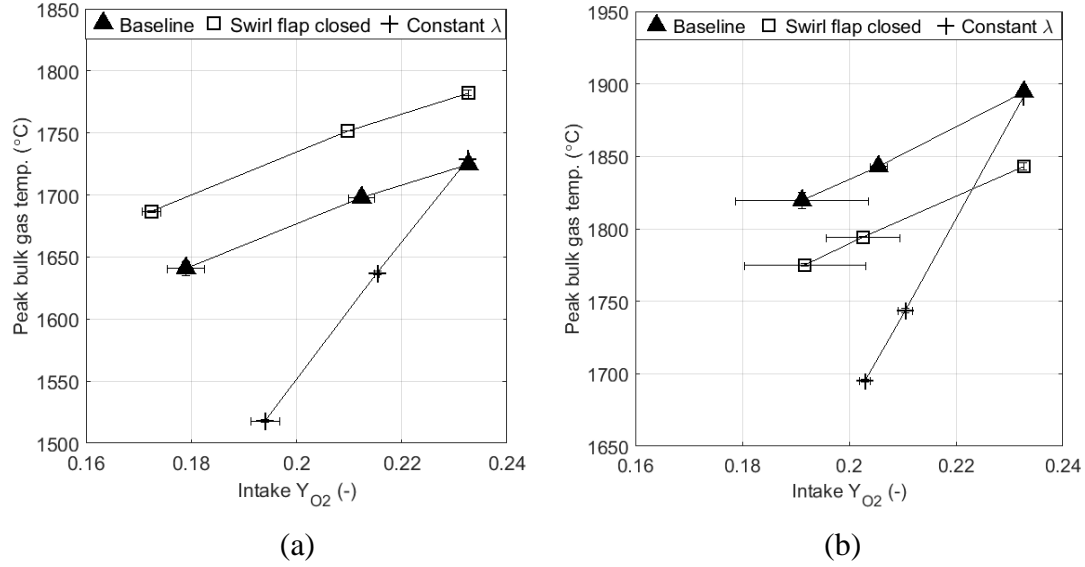


Figure 15: Peak gas bulk temperature (based on cylinder pressure signal assuming ideal gas behaviour) vs. intake oxygen mass fraction for the different EGR strategies at (a) 1500 rpm/6.8 bar nIMEP and (b) 1750 rpm/13.5 bar nIMEP load conditions.

Constant lambda EGR

The conventional application of EGR in diesel engines displaces oxygen from the intake charge, typically increasing soot emissions [3-5]. Ladommatos *et al.* [3] suggested that “additional” EGR (i.e. introducing EGR without displacing oxygen) would alleviate this problem and thus might be a better way of applying EGR in diesels. Maintaining a constant λ value as EGR is increased would indicate that a constant mass of oxygen is maintained in the cylinder relative to the fuelling regardless of EGR rate thus alleviating the negative effects of oxygen displacement during EGR application. Note that in a real (multi-cylinder) engine running with a fixed turbine geometry, the boost pressure would vary with EGR level so that for these engines ‘real’ EGR would be somewhere between the constant lambda and displacement EGR strategies examined in this work. However, where the engine uses a variable geometry turbine, as is the case in many modern vehicles, the boost pressure can be held constant and the EGR rate adjusted with the EGR valve. The constant lambda scenario is representative of this strategy.

Clearly, for a given load and speed condition, the ‘additional’ EGR approach necessitates an increase in intake mass flow rate and hence a higher intake pressure. For EGR to be driven against this pressure, the exhaust backpressure must also increase. This can be seen in Table 3, which describes the intake and exhaust backpressure conditions used to drive the EGR for the constant λ tests. The increase in pumping work associated with the ‘additional’ EGR strategy is in the range of 0.5 % to 2.5 % (Figure 5), contributing to the reduced brake efficiency shown in Figure 6. It is not certain however that these penalties in efficiency will be as profound for multi-cylinder engines where the intake and exhaust mass flow rates are proportionally increased.

The results presented in Figure 8, indicating the heat flow to the coolant, show increased sensitivity to EGR for the constant λ case compared with both the baseline and swirl flap cases, particularly at the lower speed/load condition (1500 rpm/6.8 bar nIMEP). It is thought that this increased sensitivity is caused by the increased charge density associated with the ‘additional’ EGR increasing the total heat capacity of the charge. Increasing the heat capacity will cause an additional reduction in the peak bulk gas temperature on top of that expected from EGR alone. This hypothesis is supported by the results presented in Figure 15. For all conditions, the calculated peak gas bulk temperature is seen to decrease with increasing EGR, as expected. However, the results for the constant λ case show a much more significant decrease in peak gas bulk temperature with EGR than either of the baseline and closed swirl flap cases.

The significant reduction in peak bulk gas temperature observed under constant λ operation as EGR levels are increased is interesting in light of the NO_x emissions results shown in Figure 16, which presents normalised brake specific NO_x emissions for the baseline and constant λ cases, plotted against the total intake oxygen mass and the peak bulk gas temperature. Increasing EGR rates under constant λ operation leads to a comparative increase in NO_x emissions with respect to the baseline case that is attributed by the authors to the greater oxygen content of the charge (it is assumed that despite the reduction of peak gas temperature shown in Figure 15, the local reaction zone temperatures remain sufficiently high as to generate thermal NO_x). Since no oxygen is displaced under constant λ operation, local oxygen availability is increased.

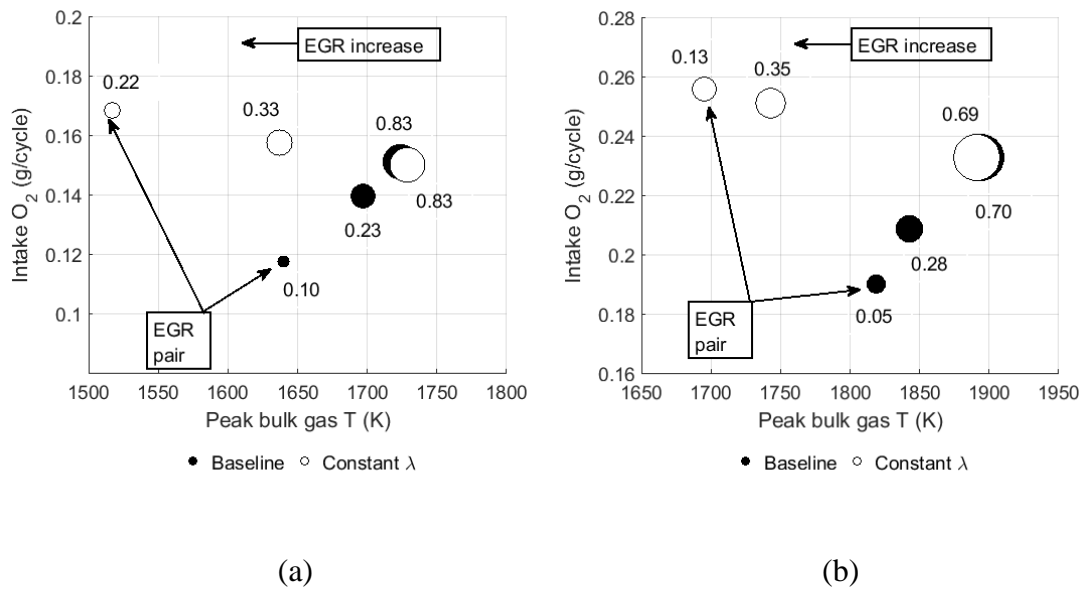


Figure 16: Intake oxygen mass vs. peak bulk gas temperature for the baseline and constant λ cases at (a) 1500 rpm/6.8 bar nIMEP and (b) 1750 rpm/13.5 bar nIMEP load conditions. The circle size indicates relative NO_x emissions and the arrows indicate constant EGR ‘pairs’.

Operating at constant λ also increases charge density compared to the ‘conventional’ EGR approach (as shown in Table 3). Increasing charge density has been shown to improve fuel–air mixing and reduce ignition delay due to improved spray atomisation

[35], [36]. This agrees well with the reduction in ignition delay that is seen for the constant λ strategy 1500 rpm/6.8 bar nIMEP case compared with the baseline case (Figures 10). Interestingly, the results presented in Figures 12 show that combustion duration for the constant λ EGR strategy is relatively insensitive to EGR rate. This contrasts sharply with the baseline and swirl flap strategy results where combustion duration was substantially increased by the addition of EGR, particularly at low load and speed. These results then suggest that the increased oxygen availability and charge density provided by the constant λ strategy is enabling a more sustained and complete combustion event for a given EGR rate. Note that reduced sensitivity of the CO and THC emissions to EGR for the constant λ case, presented in Figures 13 and 14 respectively, and the significant reduction in soot emissions at high levels of EGR compared to the baseline and swirl flap cases (Figure 9) also support this interpretation of the results and are in good agreement with the earlier work of Ladommatos *et al.* [3].

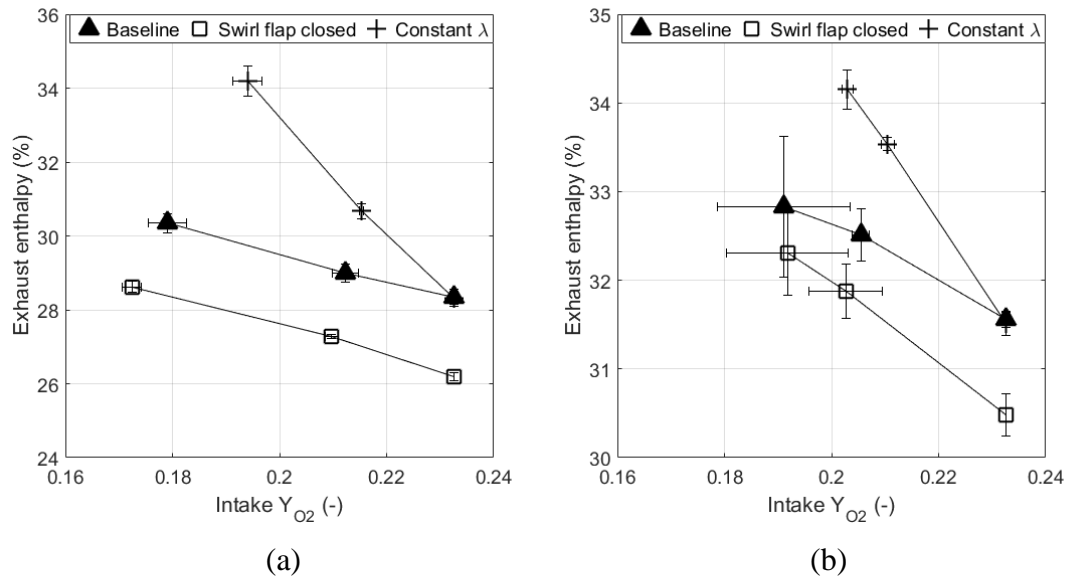


Figure 17: Exhaust enthalpy as a percentage of input energy vs. intake oxygen mass fraction for the different EGR strategies at (a) 1500 rpm/6.8 bar nIMEP and (b) 1750 rpm/13.5 bar nIMEP load conditions.

Figure 17 shows the exhaust enthalpy as a percentage of input energy against intake oxygen mass fraction for the different EGR strategies. Given approximately constant values of efficiency, pumping work, ancillary work and extraneous losses, the energy transferred to the exhaust will follow an opposite trend to the coolant heat transfer. Increasing levels of EGR are seen to increase the energy transferred to the exhaust. It is interesting to note that the exhaust enthalpy is increased under constant λ operation despite a substantial ($\sim 50^\circ\text{C}$) reduction in exhaust temperature. This is due to the fact that the total energy transferred to the exhaust is a function of both the specific enthalpy and the mass flow rate of the exhaust gases. The higher intake mass flow rate under constant λ operation, leads to an increase in the exhaust mass flow rate relative to the baseline case.

Finally, the authors note that Ricardo Hydra engine used in this work is atypical in many respects, not least in that as an unbalanced engine it is attached to a very large seismic mass, which acts as a very effective heat sink. Accordingly, the overall magnitudes of the energy flows that are determined on this engine are not expected to be representative of a production multi-cylinder. In particular, heat losses to the coolant circuit are lower than would be expected of a multi-cylinder engine and extraneous losses are substantially increased. Nonetheless, the changes in energy flow induced by variations of EGR strategy, speed and load observed in this work are expected to be indicative of real engine behaviour.

Conclusions

The effects of three different cooled high-pressure EGR strategies (baseline, closed swirl flap, and constant λ) on engine efficiency and the resulting energy flows have been studied at two speed/load conditions using a first law analysis approach on a single cylinder high speed Diesel engine.

The results for the baseline EGR strategy with constant boost pressure and reducing lambda with increasing EGR were found to be in good agreement with the literature such that increasing EGR rate was shown to increase ignition delay and combustion duration. Bulk gas temperature and NO_x emissions were reduced, as was heat transfer to the coolant. Exhaust thermal energy was increased, as were smoke and CO emissions.

Introducing EGR under higher swirl conditions induced by closing the swirl flap:

- Increased pumping work and reduced brake efficiency
- Increased heat flow to the coolant
- Reduced exhaust thermal energy

Some differences were noted between the two load conditions; for the low-load low-speed condition (1500 rpm/6.8 bar), the closed swirl flap results indicate an increase in post-ignition fuel-air mixing such that:

- Combustion duration, and smoke, CO, and THC emissions are reduced
- Peak bulk gas temperatures and NO_x emissions are increased

For the mid-load, higher-speed (1750 rpm/13.5 bar) condition, the closed swirl flap results indicate an increase in combustion duration attributed to excessive swirl levels increasing heat convection from the reaction zone leading to:

- A reduction in peak bulk gas temperature and increased smoke and CO emissions
- Increased exhaust gas temperature

The addition of EGR under conditions of constant λ increases, for any given EGR rate, the intake mass flow rate and therefore charge density, the specific heat of the charge, and the oxygen content of the charge. These changes lead to the following changes with respect to the baseline EGR strategy:

- Pumping work and exhaust thermal energy being increased
- Peak bulk gas temperature, exhaust gas temperature, and heat transfer to the coolant being reduced
- Soot, CO, and THC emissions being decreased, as was combustion duration
- NO_x emissions are higher for the same EGR rate
- Brake efficiency was reduced at low load

Finally, this work has demonstrated the extreme difficulty of obtaining accurate measurements of energy transfer to the engine coolant system at low-load. The results indicate that twenty-three repeat tests would be necessary to provide statistical certainty to these measurements at 95% confidence even when using purpose-built differential thermocouples accurate to ± 0.07 K.

References

1. Mock P. European vehicle market statistics pocketbook 2016/17. International Council on Clean Transportation, 2016.
2. Posada F, Bandivadekar A and German J. Estimated Cost of Emission Control Technologies for Light-Duty Vehicles Part 2 - Diesel. SAE paper 2013-01-0539, 2013.
3. Ladommatos N, Abdelhalim S and Zhao H. The effects of exhaust gas recirculation on diesel combustion and emissions. *Int J Engine Res* 2000; 1: 107-126.
4. Kreso AM, Johnson JH, Gratz LD, et al. A Study of the Effects of Exhaust Gas Recirculation on Heavy-Duty Diesel Engine Emissions. SAE paper 981422, 1998.
5. Akihama K, Takatori Y, Inagaki K, et al. Mechanism of the Smokeless Rich Diesel Combustion by Reducing Temperature. SAE paper 2001-01-0655, 2001.
6. Idicheria CA and Pickett LM. Effect of EGR on diesel premixed-burn equivalence ratio. *Proc Combust Inst* 2007; 31: 2931-2938.
7. Kimura S, Aoki O, Kitahara Y, et al. Ultra-Clean Combustion Technology Combining a Low-Temperature and Premixed Combustion Concept for Meeting Future Emission Standards. SAE paper 2001-01-0200, 2001.
8. Wagner RM, Green JB, Dam TQ, et al. Simultaneous Low Engine-Out NO_x and Particulate Matter with Highly Diluted Diesel Combustion. SAE paper 2003-01-0262, 2003.
9. Miles PC. The Influence of Swirl on HSDI Diesel Combustion at Moderate Speed and Load. SAE paper 2000-01-1829, 2000.
10. Dec JE and Tree DR. Diffusion-Flame / Wall Interactions in a Heavy-Duty DI Diesel Engine. SAE paper 2001-01-1295, 2001.
11. Leach F, Davy M, Weall A, et al. Comparing the Effect of a Swirl Flap and Asymmetric Inlet Valve Opening on a Light Duty Diesel Engine. SAE paper 2017-01-2429, 2017.
12. Miles PC and Andersson Ö. A review of design considerations for light-duty diesel combustion systems. *Int J Engine Res* 2016; 17: 6-15.
13. Bergin MJ, Reitz RD and Oh S. Fuel Injection and Mean Swirl Effects on Combustion and Soot Formation in Heavy Duty Diesel Engines. SAE paper 2007-01-0912, 2007.
14. Ament F, Patterson DJ and Mueller A. Heat Balance Provides Insight into Modern Engine Fuel Utilization. SAE paper 770221, 1977.
15. Alkidas AC. The Use of Availability and Energy Balances in Diesel Engines. SAE paper 890822, 1989.
16. Alkidas AC and Cole RM. The Distribution of Heat Rejection from a Single-Cylinder Divided-Chamber Diesel Engine. SAE paper 810959, 1981.
17. Heywood JB. *Internal Combustion Engine Fundamentals*. MacGraw-Hill, 1988.
18. Anderson MK, Assanis DN, and Filipi Z. First and Second Law Analyses of a Naturally-Aspirated, Miller Cycle, SI Engine with Late Intake Valve Closure. SAE paper 980889, 1998.
19. Payri F, Martin J, Garcia A, et al. Experimental and Theoretical Analysis of the Energy Balance in a DI Diesel Engine. SAE paper 2015-01-1651, 2015.
20. Dahlstrom J, Andersson O, Tuner M, et al. Experimental Comparison of Heat Losses in Stepped-Bowl and Re-Entrant Combustion Chambers in a Light Duty Diesel Engine. SAE paper 2016-01-0732, 2016.
21. Olmeda P, Martin J, Garcia A, et al. Evaluation of EGR Effect on the Global Energy Balance of a High Speed DI Diesel Engine. SAE paper 2016-01-0646, 2016.
22. Smith LA, Preston WH, Dowd G, et al. Application of a First Law Heat Balance Method to a Turbocharged Automotive Diesel Engine. SAE paper 2009-01-2744, 2009.
23. Donn C, Zulehner W, Ghebru D, et al. Experimental Heat Flux Analysis of an Automotive Diesel Engine in Steady-State Operation and During Warm-Up. SAE paper 2011-24-0067, 2011.
24. Chittick S, Swindell M and Raorane S. Analytical and Developmental Techniques Utilized in the Structural Optimization of a New Lightweight Diesel Engine. *SAE Int J Engines* 2015; 8:1960-1966. .

25. HORIBA, Motor Exhaust Gas Analyser MEXA-ONE Instruction manual, 2014.
26. AVL, AVL415S Variable sampling smoke meter operating manual, 2005.
27. Leach F, Ismail R, Davy M, et al. Comparing the Effect of Fuel/Air Interactions in a Modern High-Speed Light-Duty Diesel Engine. SAE paper 2017-24-0075, 2017.
28. AVL CONCERTO, in Application Notes. 2015.
29. Silvis WM, An Algorithm for Calculating the Air/Fuel Ratio from Exhaust Emissions. SAE paper 970514, 1997.
30. Duboc B. *The effect of fuel additives on diesel fuel delivery system and combustion performance*. PhD Thesis, University College London, UK, 2014.
31. Kook S, Bae C, Miles PC, et al. The Effect of Swirl Ratio and Fuel Injection Parameters on CO Emission and Fuel Conversion Efficiency for High-Dilution, Low-Temperature Combustion in an Automotive Diesel Engine. SAE paper 2006-01-0197, 2006.
32. Stone R. *Introduction to Internal Combustion Engines*. 4th ed. UK: Palgrave Macmillan, 2012.
33. Miles PC. Turbulent Flow Structure in Direct-Injection, Swirl-Supported Diesel Engine. In: Arcoumanis C and Kamimoto T (eds) *Flow and Combustion in Reciprocating Engines*. Berlin: Springer-Verlag, 2009.
34. Cursente V, Pacaud P and Gatellier B. Reduction of the Compression Ratio on a HSDI Diesel Engine: Combustion Design Evolution for Compliance the Future Emission Standards. SAE Int J Fuels Lubr 2009; 1:420-439.
35. Henein NA, Bhattacharyya A, Schipper J, et al. Effect of Injection Pressure and Swirl Motion on Diesel Engine-out Emissions in Conventional and Advanced Combustion Regimes. SAE paper 2006-01-0076, 2006.
36. Naber JD and Siebers DL. Effects of Gas Density and Vaporization on Penetration and Dispersion of Diesel Sprays. SAE paper 960034, 1996.
37. NIST-JANAF Thermochemical Tables [Online], <http://kinetics.nist.gov/janaf/> (Accessed 2 March 2017).
38. Larsson R and Andersson O. Lubricant thermal conductivity and heat capacity under high pressure. *Proc IMech, Part J: Journal of Engineering Tribology* 2000; 214: 337-342.

Acknowledgments

The authors would like to thank the Jaguar Land Rover Limited and University of Oxford John Fell fund for financial support. Nick Papaioannou would like to thank EPSRC for supporting his research (Grant number: 1515450). The authors would also like to thank BP International for supplying the Diesel. Nick Papaioannou would like to thank David Richardson for the valuable technical input in this work. Finally, the authors would like to thank Liyah Dholiwar for undertaking much of the engine testing and the Dept. of Engineering Science technicians and maintenance teams for facilities support.

Definitions/Abbreviations

BPV	Back Pressure Valve
CA5	Angle of 5% mass fraction burned
CA50	Angle of 50% mass fraction burned
CA90	Angle of 90% mass fraction burned

EGR	Exhaust Gas Recirculation
FBP	Final Boiling Point
FLA	First Law Analysis
FSN	Filter Smoke Number
GIMEP	Gross Indicated Mean Effective Pressure
Ignition delay	CA5 – SOLP
LHV	Lower Heating Value
MFB	Mass Fraction Burned
NIMEP	Net Indicated Mean Effective Pressure
NO _x	Nitrogen oxides
PMEP	Pumping Mean Effective Pressure
Ppm	Part per million
SOLP	Start of injection, Pilot
TDC	Top Dead Centre
THC	Total HydroCarbons
VCV	Volume Control Valve
VNT	Variable Nozzle Turbine
λ	Ratio of actual Air Fuel Ratio to Stoichiometric Air Fuel Ratio
γ	Specific Heat ratio

Appendix A

In this study the system boundary around the single cylinder diesel engine can be seen in Figure A1 and the energy balance is given by the following equation:

$$\begin{aligned} \dot{m}_f \cdot Q_{LHV} + \dot{Q}_{air} + \dot{Q}_{htr} \\ = \dot{W}_{shaft} + \dot{Q}_{cool} + \dot{Q}_{oil} + \dot{Q}_{exh} + \dot{Q}_{chem} + PW + FP\ work \\ + \dot{Q}_{ext} \end{aligned} \quad (A1)$$

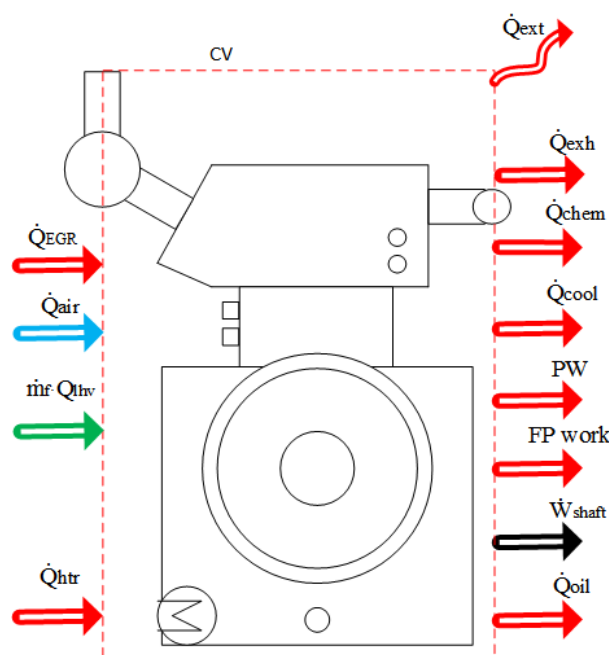


Figure A1: Control volume for the single cylinder diesel engine

The energy input from the intake air is calculated based on Equation A2. This calculation takes into account the enthalpy of the EGR constituents found in the intake manifold.

$$\begin{aligned} \dot{Q}_{air} = & \left[\left(\sum_{i=1}^n \frac{\dot{m}_i}{M_i} \cdot h_{i,man} - \sum_{i=1}^n \frac{\dot{m}_i}{M_i} \cdot h_{i,ref} \right)_{air} \right. \\ & \left. + \left(\sum_{i=1}^n \frac{\dot{m}_i}{M_i} \cdot h_{i,man} - \sum_{i=1}^n \frac{\dot{m}_i}{M_i} \cdot h_{i,ref} \right)_{EGR} \right] \end{aligned} \quad (A2)$$

The mass flow rate of species is denoted by, \dot{m}_i and the molar mass by M_i . The enthalpy of species at intake and reference conditions is denoted by h_i . The reference

conditions are specified at 298.15 K and the enthalpy of the species is calculated from JANAF polynomials [36].

The \dot{Q}_{htr} term indicates the energy input from the oil heater located in the oil sump. The energy input from the heaters has been characterised by a current clamp signal at different oil heater demands. The oil heater demand is based on the temperature difference between the set-point temperature and the oil feed temperature. Measuring the current drawn by the heaters and by knowing the mains voltage supply the power input can be calculated.

The brake power (\dot{W}_{shaft}) is calculated from the following equation:

$$\dot{W}_{shaft} = \frac{2\pi \cdot N \cdot F_{lc} \cdot L_l}{60} \quad (A3)$$

Where N is the engine speed in RPM, F_{lc} , is the load cell signal, L_l is the distance of the load cell from the centre of the crankshaft and PW is the pumping work.

The energy transferred to the coolant is calculated from Equation A4:

$$\dot{Q}_{cool} = c_{p, glycol} \cdot T_{diff(x)} \cdot \dot{v}_{(x)} \cdot \rho_{glycol} \quad (A4)$$

where $T_{diff(x)}$ is the differential thermocouple signal, $\dot{v}_{(x)}$ the measured volume flow rate of the coolant and $c_{p, glycol}$ and ρ_{glycol} are the specific heat capacity and density of ethylene glycol-water mixture for a 50% v/v concentration. X represents one of the two coolant lines (i.e. cylinder head or jacket).

The energy transferred to the oil is calculated from Equation A5.

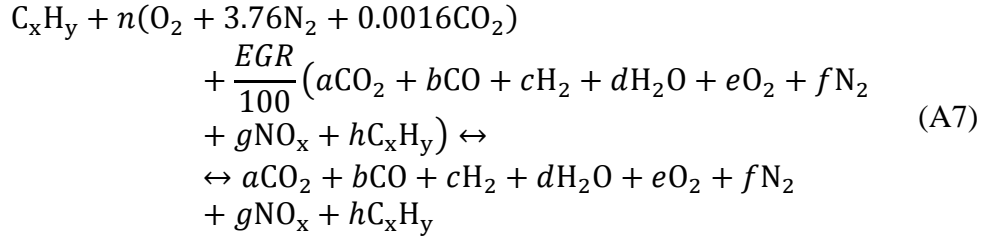
$$\dot{Q}_{oil} = c_{p, oil} \cdot (T_{out} - T_{in}) \cdot \dot{v}_{(oil)} \cdot \rho_{oil} \quad (A5)$$

The heat capacity and the density of the lubricant are based on empirical correlations derived by Larsson et al., [37] for a variety of lubricant types. The correlations used were based on the results of polyalphaolefin which is a synthetic base oil and has very similar density (810.2 kg/m^3) to the SAE 10W40 oil (819 kg/m^3) used in the single cylinder engine. This density difference leads to a 0.03% difference in the energy lost to the lubricant, which was deemed negligible.

The exhaust thermal energy is calculated from the enthalpy of the exhaust species using Equation A6.

$$\dot{Q}_{exh} = \left(\sum_{i=1}^n \frac{\dot{m}_i}{M_i} \cdot h_{i, exh} - \sum_{i=1}^n \frac{\dot{m}_i}{M_i} \cdot h_{i, ref} \right) \quad (A6)$$

The number of moles for each species is calculated from the chemical equilibrium equation of fuel and air as can be seen in Equation A7.



The number of moles of air (n), hydrogen (c), water (d) and nitrogen (f) are calculated from the iterative solution of five simultaneous equations [28], adapted to include the EGR composition. The unburned hydrocarbons found in the exhaust are assumed to have the same composition as the fuel.

The chemical energy in the exhaust (\dot{Q}_{chem}) is calculated from the oxidation energy of CO, H₂ and THC species. The equilibrium equations for CO and H₂ oxidation used can be seen in Equations A8 and A9. The energy from the unburned hydrocarbons was calculated from the calorific value of the fuel (Q_{LHV}).



The pumping work is calculated from Equation A10:

$$PW = N \cdot pmep \cdot V_s \tag{A10}$$

Where pmep is the pumping mean effective pressure and V_s is the engine swept volume. PMEP is calculated from the difference between the gross indicated mean effective pressure (gIMEP) and the net mean effective pressure (nIMEP). NIMEP is calculated over the whole engine cycle by the following equation:

$$nIMEP = \oint P dV \tag{A11}$$

GIMEP is calculated for the duration between the power and the compression strokes as seen in Equation A12:

$$gIMEP = \oint_{\text{Compression}}^{\text{Power}} P dV \tag{A12}$$

The fuel pump work (FP work) indicates the energy required to compress the fuel. The parasitic torque (T_{HPP}) used in the calculations was 8.5 Nm, based on published data of a high-pressure diesel pump [29]. The data were corrected to account for the

differences in pump types between the two studies. The ancillary work is calculated from Equation A13:

$$FP\ work = 2\pi \cdot N \cdot T_{HPP} \quad (A13)$$

Finally, the extraneous term is calculated by solving for \dot{Q}_{ext} in Equation A1